PAPER • OPEN ACCESS

Biologically inspired virtual aperture extension method of small aperture HFSWR multielement array

To cite this article: Hongbo Li *et al* 2023 *Bioinspir. Biomim.* **18** 066013

View the article online for updates and enhancements.

Bioinspiration & Biomimetics

Biologically inspired virtual aperture extension method of small aperture HFSWR multielement array

Hongbo Li[1] ⓘ, Aijun Liu[2,*], Qiang Yang[1], Changjun Yu[2] and Xuguang Yang[3]

1 Electronics and Information Engineering, Harbin Institute of Technology, Harbin, People's Republic of China
2 Information Science and Engineering, Harbin Institute of Technology at Weihai, Weihai, People's Republic of China
3 School of mathematics and Information Engineering, Long Dong University, QingYang, People's Republic of China
* Author to whom any correspondence should be addressed.

E-mail: liuaijun@hit.edu.cn

Abstract

We propose a method for extending the virtual aperture of the small aperture high-frequency surface wave radar multielement array inspired by a fly named *Ormia ochracea*. Despite the tremendous incompatibility between its ear and the incoming wavelength, *Ormia* can accurately local the sound of its host cricket. This ability benefits from the coupled structure of *Ormia*'s ears which have been modelled as a mechanical vibration system. In this paper, we first design a two-degree of freedom biologically inspired coupled system by mimicking *Ormia*'s coupled ears. We quantitatively analyze its extension capability to the array aperture and construct the received signal model of the virtual array. We then analyze its response characteristic and available frequency band. To achieve the applications of arbitrary desired frequencies, we propose a frequency conversion algorithm. Moreover, we design two multi-degree of freedom biologically inspired coupled systems for the multielement array We summarize the criteria for extending the degree of freedom and optimize these two systems to address their respective shortcomings. Numerical results give the optimal system parameters for our desired frequency and validate the frequency conversion algorithm. By comparing the radiation pattern of the inspired arrays (arrays with the proposed systems) with that of an ordinary array, we demonstrate the virtual aperture extension capability of our proposed method. We also verify the effectiveness of proposed method by processing the actual received signals of the array.

1. Introduction

Accurate source localization has been of great research interest in radar and sonar array signal processing [1–3]. Many existing localization methods, such as the convention beamforming [4] and multiple signal classification [5] methods, rely on the time differences of arrival between antenna array elements to estimate the direction of arrival (DOA). This means that these methods suffer from a fundamental limitation: their performance is directly determined by the size of the array's aperture. As a result, large aperture arrays are often necessary to ensure high-precision localization. However, a large aperture is costly and may even be infeasible in

high-frequency surface wave radar (HFSWR) applications due to the wavelength of tens or hundreds of meters, most notably in shore-based or ship-based scenarios. Therefore, the research of the small aperture array is valuable.

This paper proposes a virtual extension method of the small aperture array to enhance its performance. The method takes inspiration from a parasitic fruit fly named *Ormia Ochracea*. For population propagation, female *Ormia* must search a host cricket through the cricket's sound. This search process is hyperacute and extremely efficient, which is unexpected since the tremendous incompatibility between the wavelength of the call (about 70 mm) and the binaural spacing of the *Ormia* (about 1.5 mm) [6]. According to classical
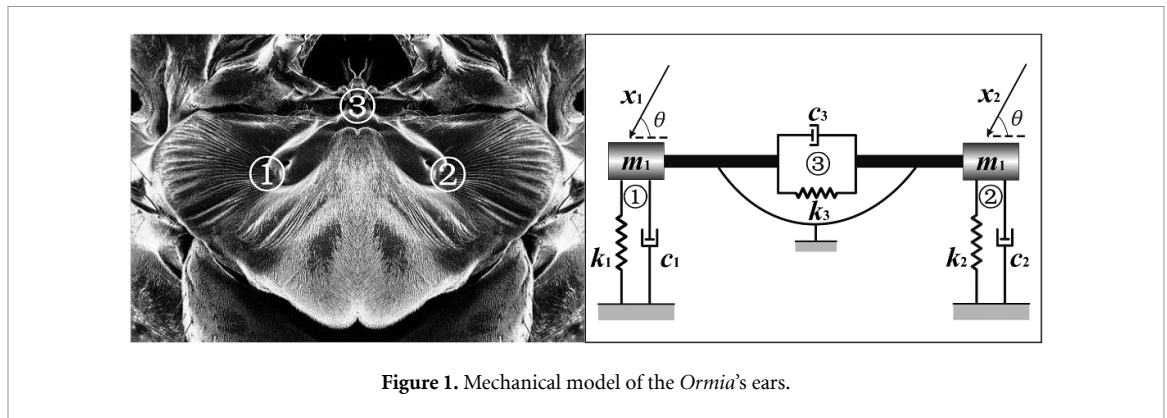
Figure 1. Mechanical model of the *Ormia*'s ears.

array signal processing theory, the *Ormia* should have a poor localization ability, such as spurious directions and poor angular resolution. However, in reality, the performance of *Ormia*'s ears is excellent, as it can easily distinguish sounds within 2°.

Miles *et al* [7] revealed that *Ormia*'s localization ability is attributed to the coupled structure between its ears. They analyzed the anatomy of the *Ormia*'s ears and modeled it as a coupled mechanical vibration model (figure 1) consisting of three spring-dashing pairs $((k_i, c_i), i = 1, 2, 3)$. In the mechanical model, the inter tympanal bridge is regarded as two steel beams coupled by a torsional spring with a stiffness coefficient of k_3 and damping coefficient of c_3. The binaural membranes, apodemes and spherical auditory nerves are considered as spring-dashing pair (k_1, c_1) and (k_2, c_2) with lumped mass m_1 and m_2.

On this basis, two research directions for small aperture array were developed. One direction focuses on studying the physical coupling circuits and designing electrically small antenna arrays that exhibit better localization performance compared to ordinary arrays with the same aperture. Behdad *et al* [8] converted the mechanical model into equivalent electrical circuits using the equivalency between mechanical elements (mass, damper, and spring) and electrical circuit elements (inductor, capacitor, resistor). They first designed a biomimetic antenna array (BMAA) by utilizing this electrical circuit as a coupling network. Subsequently, several circuit-improved and dimension-extended BMAAs were proposed [9–13]. Although these researches have been proven effective for ultra high frequency and above bands, they are unsuitable for HFSWR. For HFSWR arrays composed of antennas over ten meters long, it is costly to redesign them as BMAAs. Additionally, the electrical circuits required for such arrays are excessively large and difficult to implement.

The other direction involves studying digital coupled systems and virtually expanding the aperture of ordinary arrays through coupled processing to enhance localization performance. Akcakaya and

Nehorai [14] first applied a biologically inspired coupled (BIC) system to process signals received by antennas. They achieved high radiation performance with small aperture arrays, but the system only had two degrees of freedom. As a supplement, they extended the BIC system to be suitable for multi-antenna arrays and demonstrated its advantage for DOA estimation [15–17]. However, the description of the dimension extension process is lacking, as they only introduced a simple dimension raising of the frequency response function matrix. They neither provided a time domain model for a multi-element BIC system nor analyzed the physical mechanism behind the successful extension.

In this paper, we present a detailed design of two models for the multi-degree of freedom biologically inspired coupled (MDOF-BIC) system to a small aperture HFSWR antenna array. The system requires none coupling network and can realize a virtual expansion of the array's aperture through pure signal processing. We first analyze the inherent properties and block diagram of the *Ormia*'s hearing system. We then abstract the hearing system as a two-input two-output (TITO) system and implement a two-degree of freedom biologically inspired coupled (TDOF-BIC) system by utilizing the TITO system to process the received signals of the array. We consider the virtual expansion of the TDOF-BIC system to the array's aperture as the generation of a virtual array and establish the received signal model of this virtual array. Subsequently, we define the frequency-angle response function (FARF) and phase difference function (PDF) to analyze the response characteristics and available frequency band of the TDOF-BIC. Based on this analysis, we propose a frequency conversion algorithm to convert the available frequency band to arbitrary desired frequencies. To address multiple antenna applications, we design several models of the MDOF-BIC system and provide their common mathematical equation. By solving the responses and inherent properties of various models, we ultimately determine two successful models and summarize the criteria for extending the degree of

freedom. Furthermore, we optimize the two successful models to address their respective shortcomings. The correctness of the proposed algorithm and models is validated through numerical and experimental results.

The rest of the paper is organized as follows. In section 2, we implement the TDOF-BIC and analyze its amplification effect on the array's aperture. In section 3, we discuss the response characteristics and available frequency band of the TDOF-BIC and propose a frequency conversion algorithm. In section 4, we design several models of the MDOF-BIC and summarize the criteria for degree of freedom extension based on successful case. In section 5, we verify the proposed algorithm and models. In section 6, we provide concluding remarks.

2. TDOF-BIC algorithm

In this section, we analyze the *Ormia*'s coupled hearing system and abstract it into the digital TDOF-BIC system.

2.1. Analysis of *Ormia*'s coupled hearing system

In effect, the mechanical model (figure 1) proposed in [7] very closely represents the actual response of the coupled hearing system. According to Newton's second law, the responses of the two ends of the intertympanal bridge may be obtained by solving

$$\begin{bmatrix} m & 0 \\ 0 & m \end{bmatrix} \begin{bmatrix} \ddot{y}_1(t) \\ \ddot{y}_2(t) \end{bmatrix} + \begin{bmatrix} c_1+c_3 & c_3 \\ c_3 & c_2+c_3 \end{bmatrix} \begin{bmatrix} \dot{y}_1(t) \\ \dot{y}_2(t) \end{bmatrix}$$
$$+ \begin{bmatrix} k_1+k_3 & k_3 \\ k_3 & k_2+k_3 \end{bmatrix} \begin{bmatrix} y_1(t) \\ y_2(t) \end{bmatrix} = \begin{bmatrix} x_1(t) \\ x_2(t) \end{bmatrix} \quad (1)$$

where

- $y_1(t)$ and $y_2(t)$ are the response of the two ends of the intertympanal bridge
- $x_1(t)$ ans $x_2(t)$ are the pressures applied at the eardrums
- $(\dot{})$ denotes differentiation with respect to time t.

Since the ears are identical, we have $k_1 = k_2 = k$ and $c_1 = c_2 = c$. Suppose the pressure produced by a harmonic plane acoustic wave at the location of the pivot point is $x(t) = \exp(i\omega t)$, where ω is the frequency in radians s^{-1}. Then the pressure applied at two eardrums will be $x_1(t) = \exp[i\omega(t+\tau/2)]$ and $x_2(t) = \exp[i\omega(t-\tau/2)]$. By the well-known modal decomposition method, the responses of the intertympanal bridge may be expressed as (see the details in [7])

$$\begin{bmatrix} y_1(t) \\ y_2(t) \end{bmatrix} = \mathbf{\Phi} \begin{bmatrix} \eta_1(t) \\ \eta_2(t) \end{bmatrix}$$
$$= \begin{bmatrix} 1 & 1 \\ -1 & 1 \end{bmatrix} \begin{bmatrix} A_1 \exp(i\omega t + \varphi_1) \\ A_2 \exp(i\omega t + \varphi_2) \end{bmatrix} \quad (2)$$
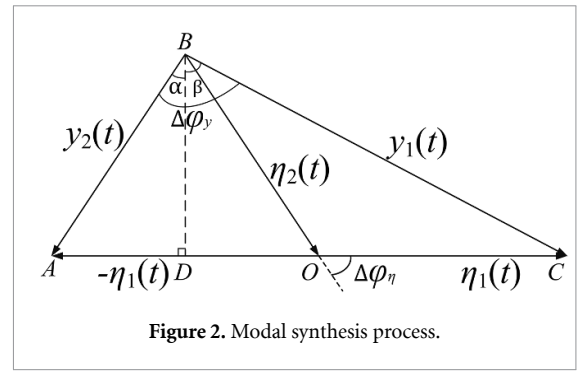

Figure 2. Modal synthesis process.

where

- $\mathbf{\Phi}$ is the modal shape matrix
- $\eta_1(t)$ and $\eta_2(t)$ are the first and second order modal responses
- A_i and $\varphi_i, i = 1, 2$ are the magnitude and phase of the *i*th order modal response

$$A_1 = 1/m \cdot \sin(\omega\tau/2) \left[\left(\omega_1^2 - \omega^2 \right)^2 + (2\omega_1\zeta_1\omega)^2 \right]^{-1/2}$$

$$A_2 = 1/m \cdot \cos(\omega\tau/2) \left[\left(\omega_2^2 - \omega^2 \right)^2 + (2\omega_2\zeta_2\omega)^2 \right]^{-1/2}$$
(3)

$$\varphi_1 = -\arctan[2\omega_1\zeta_1\omega/(\omega_1^2 - \omega^2)] + \pi/2$$
$$\varphi_2 = -\arctan[2\omega_2\zeta_2\omega/(\omega_2^2 - \omega^2)]. \quad (4)$$

In (3) and (4), ω_i and $\zeta_i, i = 1, 2$ are the *i*th natural frequency and damping ratio of the hearing system, respectively. They represent the inherent properties of the system.

$$\omega_1 = \sqrt{k/m}, \ \omega_2 = \sqrt{(k+2k_3)/m}$$
$$\zeta_1 = c/(2\omega_1 m), \ \zeta_2 = (c+2c_3)/(2\omega_2 m). \quad (5)$$

Note that $y_1(t)$ and $y_2(t)$ expressed in (2) consist of the sum of the two modal responses, and the differences in amplitude and phase between them are fairly complicated. To obtain the differences, we consider the phase of the first order modal response $\eta_1(t)$ as the reference and plot these responses in the vector space (figure 2). In figure 2, $\Delta\varphi_\eta$ represents the phase difference between the two modal responses $\eta_1(t)$ and $\eta_2(t)$, while $\Delta\varphi_y$ represents the phase difference between the responses $y_1(t)$ and $y_2(t)$. Let $\angle ABD = \alpha$, $\angle DBC = \beta$, then we have $\Delta\varphi_y = \alpha + \beta$. Define A_{y1} and A_{y2} as the lengths (or say amplitudes) of the responses $y_1(t)$ and $y_2(t)$, through trigonometric operations, we get

$$A_{y1} = \left[(A_2 \sin \Delta\varphi_\eta)^2 + (A_1 + A_2 \cos \Delta\varphi_\eta)^2 \right]^{1/2}$$

$$A_{y2} = \left[(A_2 \sin \Delta\varphi_\eta)^2 + (A_1 - A_2 \cos \Delta\varphi_\eta)^2 \right]^{1/2}$$

$$\Delta A_y = \frac{A_{y1}}{A_{y2}} = \left[\frac{\sin^2 \Delta\varphi_\eta + (\Delta A_\eta + \cos \Delta\varphi_\eta)^2}{\sin^2 \Delta\varphi_\eta + (\Delta A_\eta - \cos \Delta\varphi_\eta)^2} \right]^{1/2}$$
(6a)

$$\tan\alpha = (A_1 - A_2\cos\Delta\varphi_\eta)/(A_2\sin\Delta\varphi_\eta)$$
$$\tan\beta = (A_1 + A_2\cos\Delta\varphi_\eta)/(A_2\sin\Delta\varphi_\eta)$$
$$\tan\Delta\varphi_y = 2\Delta A_\eta\sin\Delta\varphi_\eta/(1 - \Delta A_\eta^2) \quad (6b)$$

where

- $\Delta A_\eta = A_1/A_2$ is the amplitude difference of the modal responses $\eta_1(t)$ and $\eta_2(t)$
- ΔA_y is the amplitude difference of the actual responses $y_1(t)$ and $y_2(t)$
- A_1 and A_2 are the lengths (or say amplitudes) of the vector $\eta_1(t)$ and $\eta_2(t)$

If the hearing system is uncoupled, the values of c_3 and k_3 should be zero, resulting in $\omega_1 = \omega_2$, $\zeta_1 = \zeta_2$, $\Delta A_\eta = \tan(\omega\tau/2)$ and $\Delta\varphi_\eta = \pi/2$. From this, we can deduce that $\Delta A_y = \Delta A_x = 1$ and $\Delta\varphi_y = \Delta\varphi_x = \omega\tau$, where ΔA_x and $\Delta\varphi_x$ represent the difference in amplitude and phase between $x_1(t)$ and $x_2(t)$.

For the coupled hearing system, however, $\omega_1 < \omega_2$, $\zeta_1 < \zeta_2$. This results in $A_2 < A_1$ and $\Delta\varphi_\eta \neq \pi/2$. Consequently, based on (6), we can derive that $\Delta A_y > \Delta A_x$ and $\Delta\varphi_y > \Delta\varphi_x$, which demonstrates that the hearing system can amplify the difference in amplitude and phase between the signals.

To quantify this amplification, we define the amplitude difference gain G_A and phase difference gain G_φ as

$$G_A = \Delta A_y/\Delta A_x = \Delta A_y$$
$$G_\varphi = \Delta\varphi_y/\Delta\varphi_x = \Delta\varphi_y/(\omega\tau). \quad (7)$$

2.2. Implement of the TDOF-BIC

Considering the targeted application, we now convert the physical hearing system to the digital TDOF-BIC system. We first perform the Fourier transform on (1) and utilize the modal decomposition solution in the frequency domain

$$Y_1(\omega) = \frac{(X_1(\omega) + X_2(\omega))/(2m)}{\omega_2^2 - \omega^2 + 2i\omega_2\zeta_2\omega}$$
$$+ \frac{(X_1(\omega) - X_2(\omega))/(2m)}{\omega_1^2 - \omega^2 + 2i\omega_1\zeta_1\omega}$$
$$Y_2(\omega) = \frac{(X_1(\omega) + X_2(\omega))/(2m)}{\omega_2^2 - \omega^2 + 2i\omega_2\zeta_2\omega}$$
$$- \frac{(X_1(\omega) - X_2(\omega))/(2m)}{\omega_1^2 - \omega^2 + 2i\omega_1\zeta_1\omega} \quad (8)$$

where

- $Y_1(\omega)$ and $Y_2(\omega)$ are the Fourier transforms of $y_1(t)$ and $y_2(t)$
- $X_1(\omega)$ and $X_2(\omega)$ are the Fourier transforms of $x_1(t)$ and $x_2(t)$.

Let $H_1(\omega)$ and $H_2(\omega)$ be given by (9), then the system block diagram of the hearing system is illustrated in figure 3.
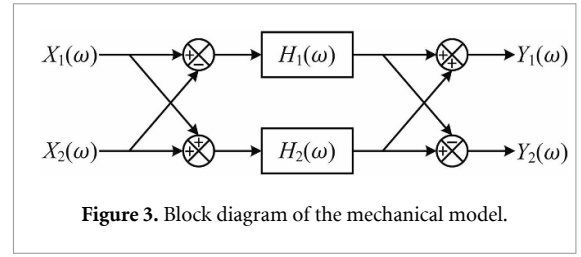

Figure 3. Block diagram of the mechanical model.

$$H_1(\omega) = \frac{1/(2m)}{\omega_1^2 - \omega^2 + 2i\omega_1\zeta_1\omega}$$
$$H_2(\omega) = \frac{1/(2m)}{\omega_2^2 - \omega^2 + 2i\omega_2\zeta_2\omega}. \quad (9)$$

The block diagram illustrates that the hearing system can be abstracted as a digital TITO system. To implement the TDOF-BIC system, we utilize the TITO system to process the signals received by the antenna arrays (refer to figure 4). In figure 4, the input signals $x_1(t)$ and $x_2(t)$ are the received signals (incident from θ_{in}) of the two-antenna array with d_{in} antenna spacing. The output signals $y_1(t)$ and $y_2(t)$ are the responses of the TITO system, which are equivalent to the received signals (incident from θ_{out}) of a virtual array with d_{out} antenna spacing. $h_1(t)$ and $h_2(t)$ are the inverse Fourier transform of the $H_1(\omega)$ and $H_2(\omega)$.

2.3. Effect analysis of the TDOF-BIC

Under the far-field radiation and narrow-band uncorrelated signal assumption, the received signal vector of the actual two-antenna array is

$$\boldsymbol{X}(t) = \boldsymbol{A}(\theta)\boldsymbol{S}(t) + \boldsymbol{e}(t) \quad (10)$$

where

- $\boldsymbol{X}(t) = [x_1(t), x_2(t)]^{\mathrm{T}}$ is the received signal vector of the array
- $\boldsymbol{S}(t) = [s_1(t), \ldots, s_N(t)]^{\mathrm{T}}$ is the incoming signal vector, with N as the number of sources
- $\boldsymbol{A}(\theta) = [\boldsymbol{a}(\theta_1), \ldots, \boldsymbol{a}(\theta_N)]$ is the array manifold matrix, with θ_n as the azimuth of the nth source
- $\boldsymbol{a}(\theta_n) = [\exp(i\omega\tau_n/2), \exp(-i\omega\tau_n/2)]^{\mathrm{T}}$ for the array
- $\tau_n = d_{in}\sin\theta_n/c$, with d_{in} and c are the antenna spacing and light speed, respectively
- $\boldsymbol{e}(t)$ is the additive white Gaussian noise with zero-mean and variance σ^2.

As mentioned in section 2.2, we consider the output vector $\boldsymbol{Y}(t) = [y_1(t), y_2(t)]^{\mathrm{T}}$ as the received signals of a virtual antenna array and establish its signal model as

$$\boldsymbol{Y}(t) = \mathrm{BIC}[\boldsymbol{X}(t)] = \mathrm{BIC}[\boldsymbol{A}(\theta)\boldsymbol{S}(t)] + \mathrm{BIC}[\boldsymbol{e}(t)] \quad (11)$$

where $\mathrm{BIC}[\cdot]$ refers to the coupled processing of the signals by the TDOF-BIC.
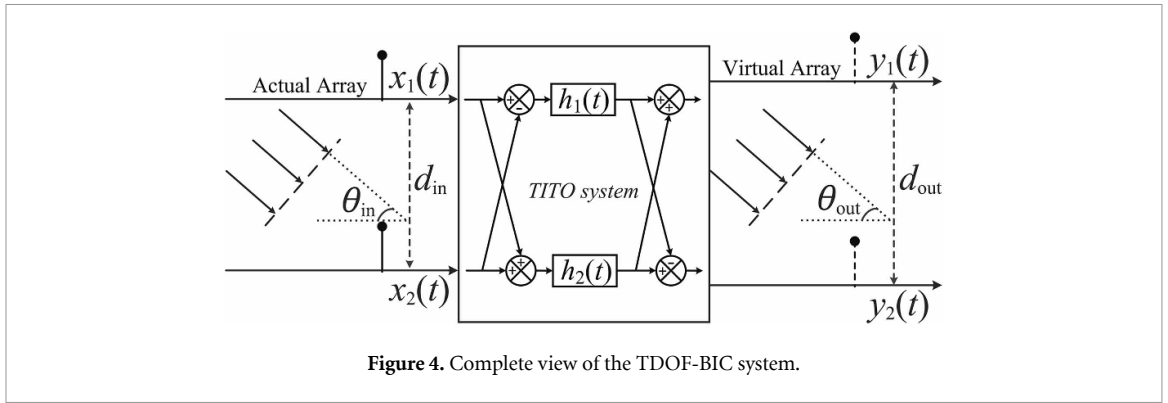
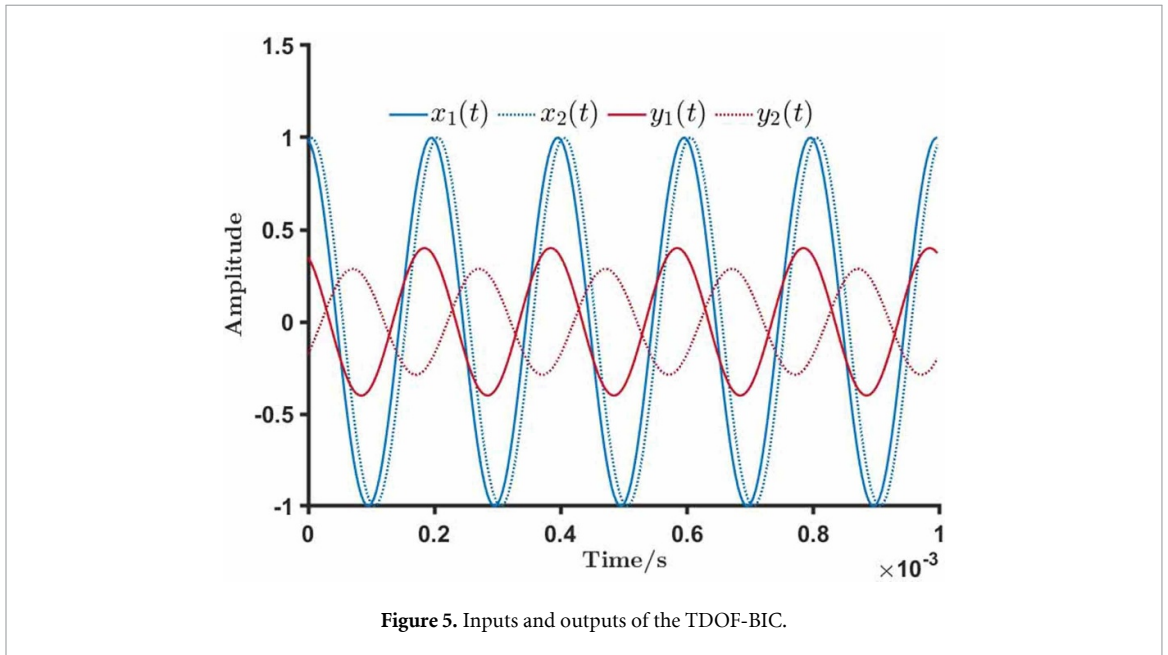**Figure 4.** Complete view of the TDOF-BIC system.

Figure 5. Inputs and outputs of the TDOF-BIC.

Since the signal $S(t)$ and noise $e(t)$ are independent, the coupled processing follows the distributive law. Therefore, we separate it into the signal and noise parts for further analysis.

(1) Signal Part: The TDOF-BIC system, being based on the same block diagram as the hearing system, retains the amplitude difference gain G_A and phase difference G_φ for the input signals. This indicates that the coupled processing of the TDOF-BIC will alter the array manifold (or create a virtual array), so we have

$$\mathrm{BIC}\left[\boldsymbol{A}\left(\theta\right)\boldsymbol{S}\left(t\right)\right] = \tilde{\boldsymbol{A}}\left(\theta\right)\boldsymbol{S}\left(t\right) \tag{12}$$

where

- $\tilde{\boldsymbol{A}}(\theta) = [\tilde{\boldsymbol{a}}(\theta_1), \ldots, \tilde{\boldsymbol{a}}(\theta_N)]$ is the virtual array manifold matrix
- $\tilde{\boldsymbol{a}}(\theta) = [G_A \exp(i\omega\tilde{\tau}/2), \exp(-i\omega\tilde{\tau}/2)]^{\mathrm{T}}$
- $\tilde{\tau} = G_\varphi \tau$.

Consider that $\tau = d_{\mathrm{in}} \sin\theta/c$, and the estimated parameter in source localization is the angle θ, it is reasonable to maintain the angle during the coupled processing. Hence, we have $\theta_{\mathrm{in}} = \theta_{\mathrm{out}}$, $d_{\mathrm{out}} = G_\varphi d_{\mathrm{in}}$ (in

figure 4), and $\tilde{\tau} = d_{\mathrm{out}} \sin\theta/c$. This demonstrates that the coupled processing of the TDOF-BIC system virtually expands the aperture of the actual array. It is noteworthy that the phase difference gain G_φ can also be regarded as the array aperture gain. Since it is influenced by the incident angle of the signal, we redefine its domain as

$$G_\varphi = \Delta\varphi_y/(\omega\tau) = \Delta\varphi_y \cdot c/(\omega d_{\mathrm{in}} \sin\theta), \qquad \theta \neq 0° \tag{13}$$

(2) Noise Part: As stated in (1), the TDOF-BIC system is also a linear system. So for the white noise, it will be transformed into colored noise through the coupled processing.

$$\mathrm{BIC}\left[\boldsymbol{e}\left(t\right)\right] = \tilde{\boldsymbol{e}}\left(t\right) \tag{14}$$

where $\tilde{\boldsymbol{e}}(t)$ is the Colored Gaussian Noise.

Therefore, the final signal model of the virtual array is

$$\boldsymbol{Y}(t) = \mathrm{BIC}\left[\boldsymbol{X}(t)\right] = \tilde{\boldsymbol{A}}\left(\theta\right)\boldsymbol{S}\left(\theta\right) + \tilde{\boldsymbol{e}}(t). \tag{15}$$

See figure 5 for the inputs and responses of the TDOF-BIC system. The inputs are incident from 30°
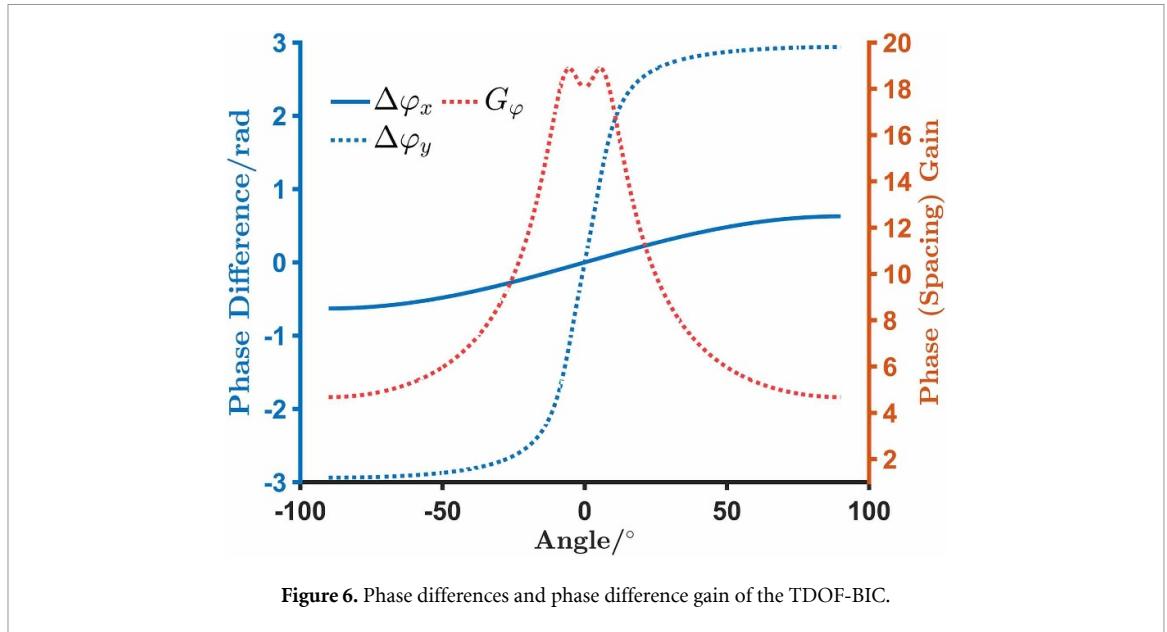
Figure 6. Phase differences and phase difference gain of the TDOF-BIC.

relative to the direction that is tangent to the plane of the array. Note that the noise has been disregarded to ensure clear and visual results. We observe that the system amplifies the difference in amplitude and phase between the signals, equivalent to extend the virtual aperture of the array. Figure 6 illustrates the phase differences $\Delta\varphi_x$, $\Delta\varphi_y$ and phase difference gain G_φ at various incident angles. There exists a one-to-one correspondence between the incident angle and phase difference, confirming that the outputs of the TDOF-BIC can be utilized for source localization. It is observed that the gain increases as the angle approaches $0°$. The system has no amplification effect at $0°$ since the absence of phase difference between the inputs. The two figures are considered for the 5 kHz signal using the parameters (mass, spring and damping) experimentally obtained in [7], and the antenna spacing d_{in} takes one-tenth of the wavelength. The amplitude difference is not provided as it is not the focus point of this paper.

3. Frequency conversion algorithm design

In this section, we analyze the response characteristics of the TDOF-BIC system and propose a specific frequency conversion algorithm to convert the system's available frequency band to arbitrary desired frequencies.

3.1. Response characteristics of the TDOF-BIC

We first derive the transfer functions of the TDOF-BIC by directly solving (1) in the transform domain (for more details, refer to [16]).

$$H_1(\omega,\theta) = \left[D(i\omega)e^{i\kappa\sin\theta} - N(i\omega)e^{-i\kappa\sin\theta}\right]/P(i\omega)$$
$$H_2(\omega,\theta) = \left[D(i\omega)e^{-i\kappa\sin\theta} - N(i\omega)e^{i\kappa\sin\theta}\right]/P(i\omega)$$
$$(16)$$

where

- $P(i\omega) = D^2(i\omega) - N^2(i\omega)$ is the characteristic function
- $D(i\omega) = m\omega^2 + i(c + c_3)\omega + k + k_3$
- $N(i\omega) = ic_3\omega + k_3$ (coupling term)
- $\kappa = \pi d_{in}/\lambda$.

Observe that the transfer function between the inputs and outputs is influenced not only by the frequency but also by the incident angle. So we rename it as the FARF. We also introduce the PDF to analyze the phase difference between the responses at different frequencies and angles

$$P_D(\omega,\theta) = \text{Arg}\left[H_1(\omega,\theta)/H_2(\omega,\theta)\right] \quad (17)$$

where $\text{Arg}[\cdot]$ represents to find the phase angle in $[]$.

3.2. Analysis of the response characteristics

There are two other noteworthy properties of mechanical damping systems: damped frequency ω_d and maximum response frequency ω_b [18]

$$\omega_d = \omega_n\sqrt{1-\zeta^2}$$
$$\omega_b = \omega_n\sqrt{1-2\zeta^2} \quad (18)$$

where ω_n and ζ represent the natural frequency and damping ratio, respectively. Since the TDOF-BIC system is abstracted from the mechanical system, it inherits these properties.

Still select the parameters in [7], figure 7 presents the response characteristics of the TDOF-BIC system by FARF. We only provide the result of $H_1(\omega,\theta)$ since $H_1(\omega,\theta)$ and $H_2(\omega,\theta)$ exhibit symmetry about $\theta = 0°$. We observe that with a fixed incident angle, the frequency-angle response of the TDOF-BIC initially increases and then decreases as the frequency

Figure 7. FARF of the TDOF-BIC system. (a) Three-dimensional map. (b) Contour map.
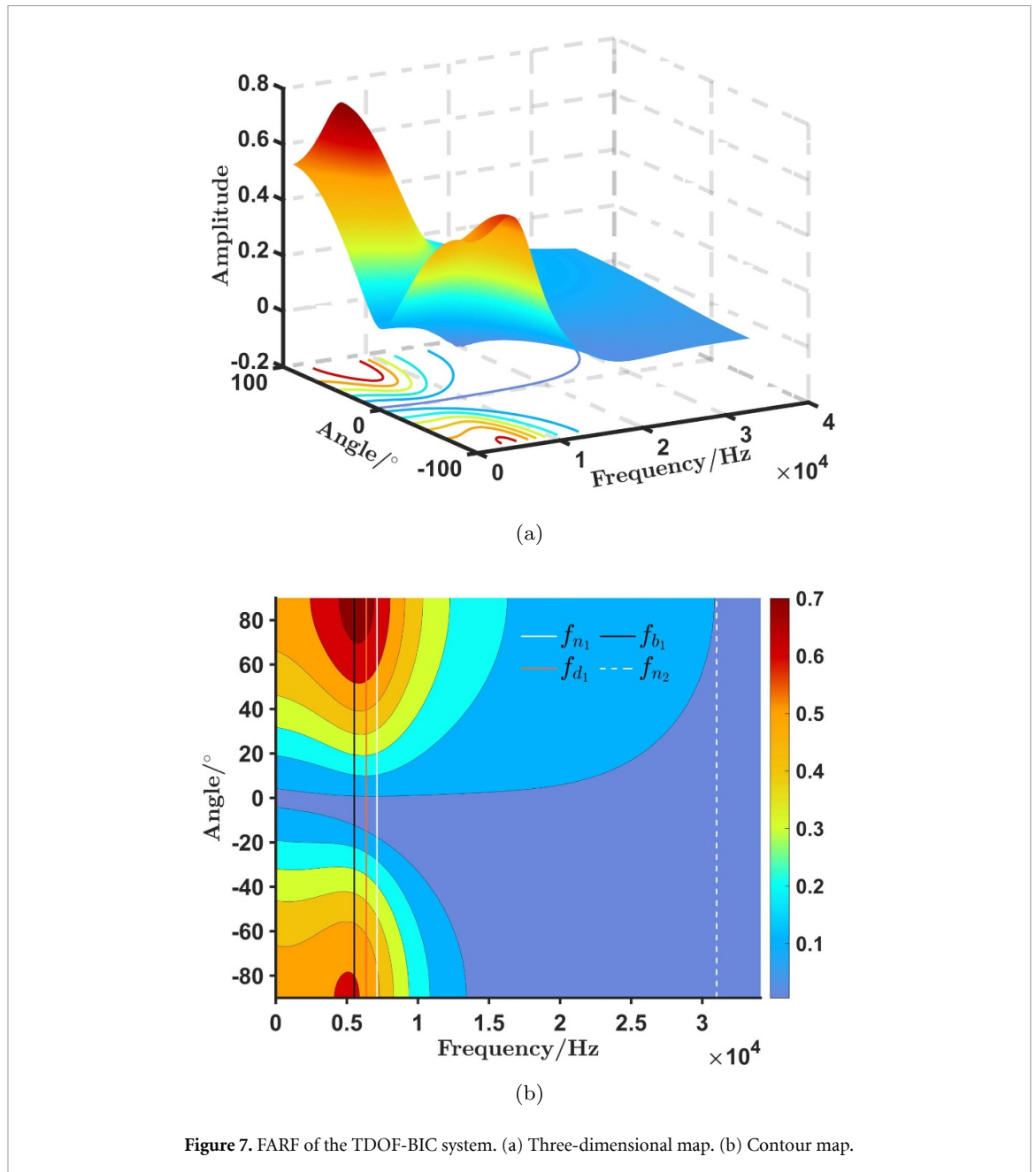
increases. The contour map illustrates that the amplitude of the response at the first natural frequency is significantly larger than that at the second natural frequency. Its maximum value is located near the first maximum response frequency and decreases as the angle approaches $0°$.

Figure 8 plots the PDF of the TDOF-BIC at various frequencies and angles. In the low-frequency range, the phase difference and incident angle share the same symbol, indicating a correct correspondence. While in the high-frequency range, the symbols of them are opposite, indicating that the TDOF-BIC system is unavailable. The frequency at which the symbol feature changes is defined as the jump frequency, denoted by f_j. We select several specific frequency points to slice the three-dimensional map and present the results in figure 8(b). Due to the

sampling rate limitation, we can only determine that $f_j \in [f_j^-, f_j^+]$. Within the $[0, f_j^-]$ (available) band, the phase differences under large incident angles ($[-90°, -30°]$ and $[30°, 90°]$) flatten while the phase differences under small incident angles ($[-30°, 30°]$) steepen as the frequency rises. This may lead to an ambiguity correspondence relationship between the incident angle and virtual aperture, which hinders subsequent source localization.

To determine the precise jump frequency f_j, we expand (17) and calculate its partial derivation with respect to the incident angle

$$
\begin{aligned}
\dot{P}_D(\omega, \theta) &= \partial P_D(\omega, \theta) / \partial \theta \\
&= \Gamma \left[\left(\omega_1^2 - \omega^2 \right) \left(\omega_2^2 - \omega^2 \right) + 4\omega_1 \zeta_1 \omega_2 \zeta_2 \omega^2 \right]
\end{aligned}
\tag{19}
$$

(a)

(b)

Figure 8. PDF of the TDOF-BIC system. (a) Three-dimensional map. (b) Slice map.
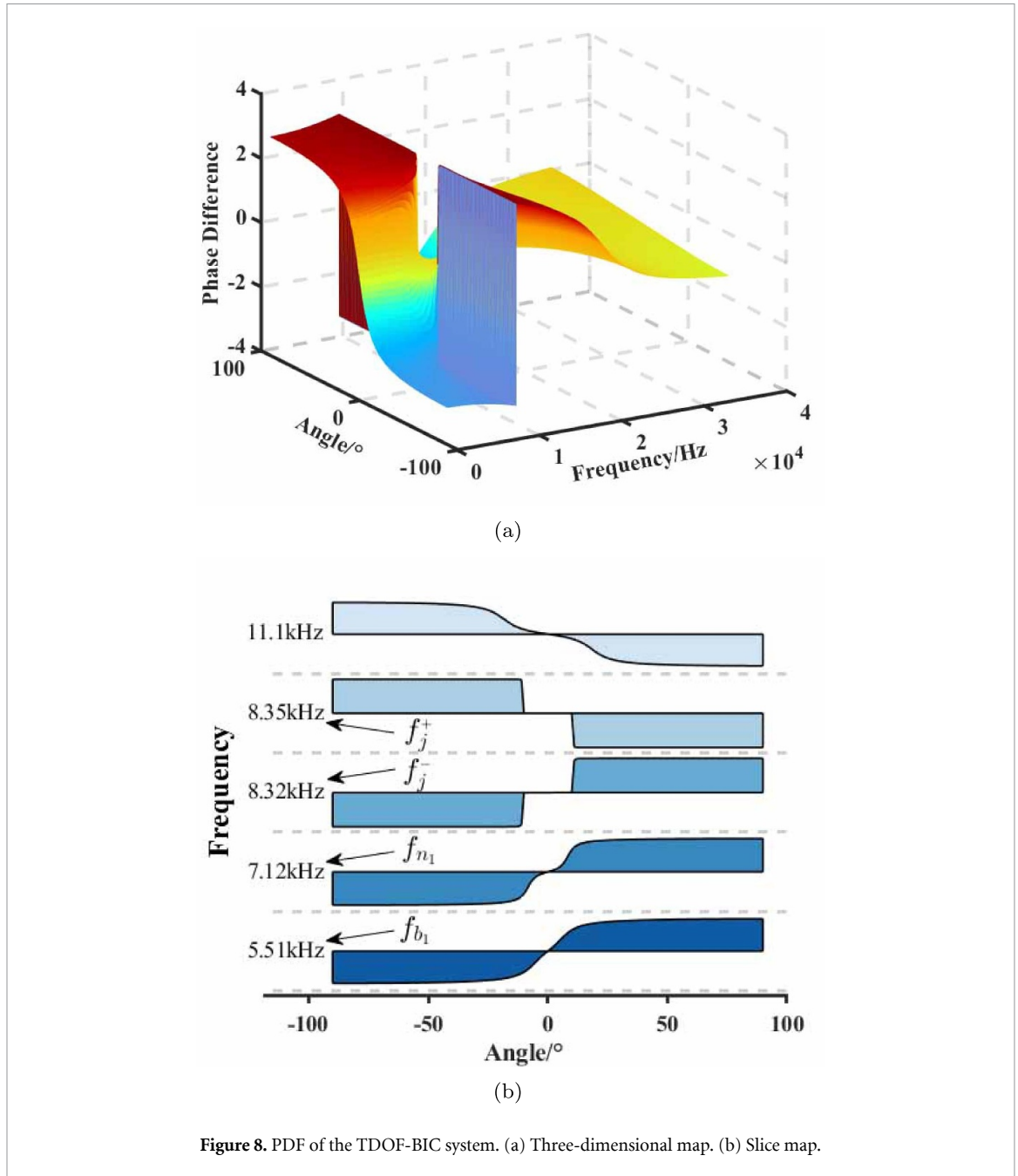
where

- $\Gamma = \frac{2(1+E\tan^2 A)\cos\theta}{(1+B^2)(D-E\tan^2 A)^2 \cos^2 A}$ is always positive
- $A = \kappa\sin\theta$
- $B = \left[2((\omega_2^2 - \omega^2)(\omega_1^2 - \omega^2) + 2\omega_1\zeta_1\omega_2\zeta_2)\tan A\right] / (D - E\tan^2 A)$
- $D = (\omega_1^2 - \omega^2)^2 + (2\omega_1\zeta_1\omega)^2$
- $E = (\omega_2^2 - \omega^2)^2 + (2\omega_2\zeta_2\omega)^2$.

By making the partial derivation equal to zero, we obtain two possible solutions for the jump frequency

$$\omega_{j_1}^2 = \frac{b - \sqrt{b^2 - 4\omega_1^2\omega_2^2}}{2}$$

$$\omega_{j_2}^2 = \frac{b + \sqrt{b^2 - 4\omega_1^2\omega_2^2}}{2} \qquad (20)$$

where $b = \omega_1^2 + \omega_2^2 - 4\omega_1\zeta_1\omega_2\zeta_2$. Figure 8(b) shows that the slope of $P_D(2\pi f_j^-, \theta)$ is greater than zero while the slope of $P_D(2\pi f_j^+, \theta)$ is less than zero. So we determine the final solution of the jump frequency is $f_j = \omega_{j_1}/(2\pi)$.

3.3. Frequency conversion algorithm design

We now convert the available band of the TDOF-BIC to desired frequencies based on the response characteristics. This means to alter the system parameters, namely the mass, spring and damping constants in the mechanical system. Although we retain the names of these parameters in the digital TDOF-BIC system, they no longer have physical significance. Naturally, we aim to maximize the response amplitude, so we set the desired frequency equal to the

first maximum response frequency. In addition, to prevent any potential ambiguity between the incident angle and virtual aperture, the desired frequency should be as far away from the jump frequency as possible. Therefore, we formulate the problem as an optimization problem to determine the maximum jump frequency given the predetermined desired frequency

$$
\begin{aligned}
\text{maximum} \quad & \omega_j(m,k,k_3,c,c_3) \\
\text{subject to} \quad & \omega_g = \omega_1\sqrt{1-2\zeta_1^2} \\
& b^2 - 4\omega_1^2\omega_2^2 \geqslant 0 \\
& 1 - 2\zeta_1^2 > 0 \\
& m,k,k_3,c,c_3 > 0
\end{aligned}
\tag{21}
$$

where ω_g represent the desired frequency we give.

To ensure acceptable initial values, we first modify the available band at the macro level (such as shifting it from the kHz to MHz range). This modification can be achieved by adjusting the first natural frequency.

In addition, we derive the amplitude response of $H_1(\omega,\theta)$ as

$$
|H_1(\omega,\theta)|
$$

$$
= \left[\frac{(u\cos A + V\sin A)^2 + (U\cos A - v\sin A)^2}{m^2(U^2+u^2)(V^2+v^2)}\right]^{1/2}
\tag{22}
$$

where

- $U = \omega_1^2 - \omega^2$, $V = \omega_2^2 - \omega^2$
- $u = 2\omega_1\zeta_1\omega$, $v = 2\omega_2\zeta_2\omega$
- $A = \kappa\sin\theta$.

Notably, if the operating frequency ω is scaled with the same constant as the natural frequencies ω_1 and ω_2, $|H_1(\omega,\theta)|$ is unaffected by change in the mass term while significantly influenced by changes in the stiffness terms. Therefore, we propose the initial value selection scheme as: (1) maintain k and k_3; (2) adjust m to convert the first natural frequency; (3) adjust c to satisfy the first equality constraint in (21); (4) adjust c_3 to maintain ζ_2.

4. MDOF-BIC system

In this section, we establish two viable models of the MDOF-BIC system and derive their common mathematical equation. We also summarize the criteria for expanding the degrees of freedom.

4.1. Design of the MDOF-BIC models

For the sake of convenience, we first simplify the TDOF-BIC system to a simple model (figure 9(a)). In the figure, the white circles represent the receiving antennas and the black circle represents the coupling item between the two antennas. By imitating the TDOF-BIC model, we establish a series of construct models for the MDOF-BIC, including the chain model, ring model, star model, fully connected model and combined model. See figures 9(b)–(f) as these models, and they already contain all possible models of the MDOF-BIC system.

Inspired by (1), we summarize the common mathematical model for the MDOF-BIC systems with N antennas in (23). Here, p_i represents the number of the coupling terms connected to the ith antenna, and q_{ij} ($i \neq j$) represents whether the ith and jth antennas are connected by the coupling term (1 for yes, 0 for no).

$$
\begin{bmatrix} m & & & 0 \\ & m & & \\ & & \ddots & \\ 0 & & & m \end{bmatrix}
\begin{bmatrix} \ddot{y}_1(t) \\ \ddot{y}_2(t) \\ \vdots \\ \ddot{y}_N(t) \end{bmatrix}
+
\begin{bmatrix} c+p_1c_3 & q_{12}c_3 & & q_{1N}c_3 \\ q_{21}c_3 & c+p_2c_3 & & q_{2N}c_3 \\ & & \ddots & \\ q_{N1}c_3 & q_{N2}c_3 & & c+p_Nc_3 \end{bmatrix}
\begin{bmatrix} \dot{y}_1(t) \\ \dot{y}_2(t) \\ \vdots \\ \dot{y}_N(t) \end{bmatrix}
+
\begin{bmatrix} k+p_1k_3 & q_{12}k_3 & & q_{1N}k_3 \\ q_{21}k_3 & k+p_2k_3 & & q_{2N}k_3 \\ & & \ddots & \\ q_{N1}k_3 & q_{N2}k_3 & & k+p_Nk_3 \end{bmatrix}
\begin{bmatrix} y_1(t) \\ y_2(t) \\ \vdots \\ y_N(t) \end{bmatrix}
=
\begin{bmatrix} x_1(t) \\ x_2(t) \\ \vdots \\ x_N(t) \end{bmatrix}.
\tag{23}
$$

Taking $N=4$ as an example, we solve the responses of various MDOF-BIC models by the modal decomposition method. The results show that only the star model and fully connected model achieve the ideal phase difference amplification (or say virtual aperture extension) of the multielement array.

In figure 10, by comparing the time responses of several models, we illustrate the assessment criterion for 'ideal phase difference amplification'. The parameters used in the figure are consistent with those in section 2.3, and the signal is still incident from 30° with 5 kHz frequency. We imply that the phase relationship of the inputs is $\varphi_{x_1} > \varphi_{x_2} > \varphi_{x_3} > \varphi_{x_4}$, where the symbol '>' denotes the phase advance. For the accuracy of the subsequent source location algorithm, the responses should still maintain this phase relationship. That is to say, the 'ideal phase difference amplification' not only needs to amplify the phase difference of adjacent antennas but also ensure that the phase relationship $\varphi_{y_1} > \varphi_{y_2} > \varphi_{y_3} > \varphi_{y_4}$ is satisfied. As can be seen from the dashed box in

Figure 9. Simple models of the (a) TDOF-BIC and (b)∼(f) MDOF-BIC system. (b) Chain, (c) Ring, (d) Star, (e) Fully Connected and (f) Combined models of the MDOF-BIC.

Figure 10. Time responses of various models of the MDOF-BIC. (a) Star. (b) Fully connected. (c) Ring. (d) Combined.

figure 10, only the star model and the fully connected model meet the criteria. The chain model is omitted since the ring model and combined model are sufficiently representative.

Figure 11 shows the phase difference and phase difference (array aperture) gain between adjacent antennas of the star model, with the parameters being the same as figure 10. Combined with figure 10(a), we observe that the star model has large response amplitudes and aperture gains. Compared with the input amplitude (one), the response amplitude of the first and last antennas are almost invariant, and of the other antennas are only reduced by about half. At small incident angles, it has a tremendous average aperture gain of about 20 times. While at large angles the situation is quite different, the aperture gains are only 1.5 times, especially for the first and last spacing interval ($G_{y_{12}}$ and $G_{y_{34}}$). Note that the break point in the vicinity of 0° in figure 11(b) is due to G_φ in (13) is undefined at 0°.

Figure 11. (a) Phase difference and (b) phase difference gain between adjacent antennas of the star model.

Figure 12. (a) Phase difference and (b) phase difference gain between adjacent antennas of the fully connected model.
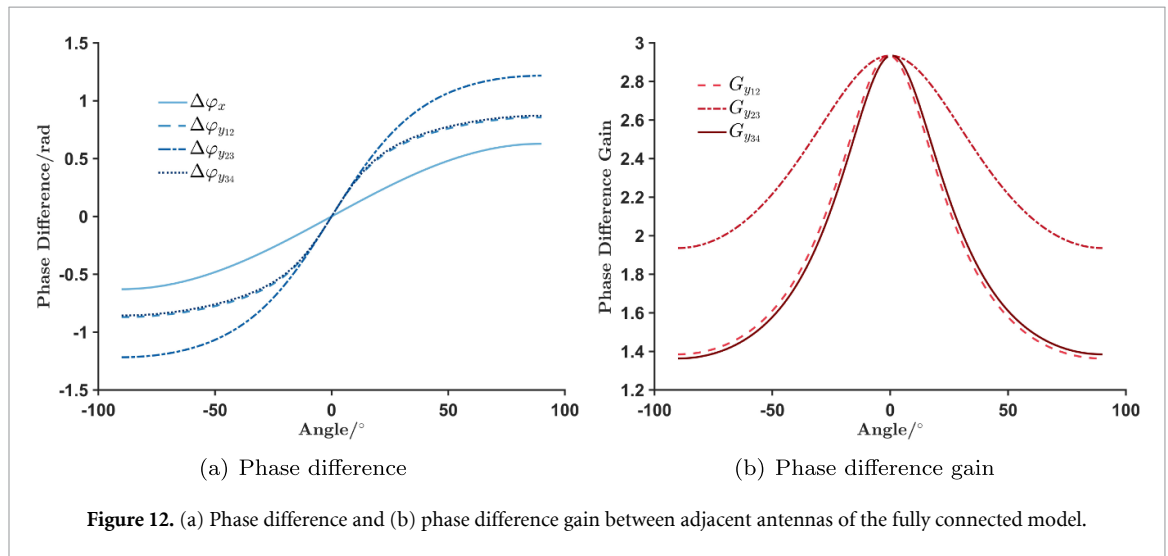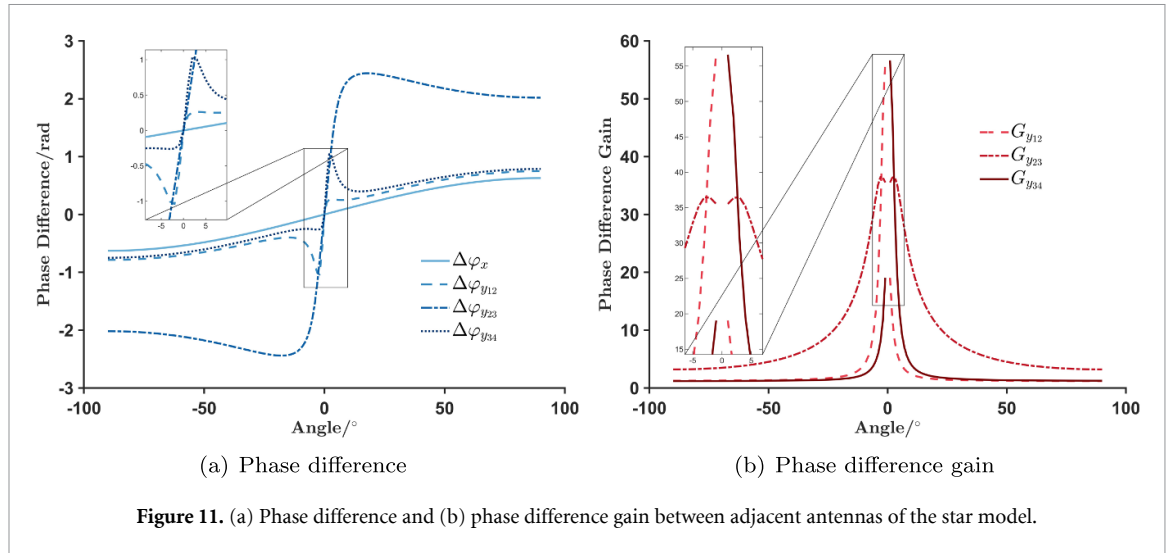
Figure 12 depicts the phase difference and phase difference (array aperture) gain between adjacent antennas of the fully connected model. The parameters are the same as those in figure 10. Combined with figure 10(b), the fully connected model has poor response amplitudes, about one-twentieth of the input amplitude. The average aperture gains of it are also modest, about 2 times. The good thing is that the difference between the response amplitudes of each antenna is not significant, and the aperture gains vary gently at the different spacing intervals and incident angles.

4.2. Criteria for the expansion of degrees of freedom

Based on the two success models, we analyze the expansion criterion from TDOF to MDOF. By writing (23) in matrix form and removing the damping term, we get the undamped equation of the MDOF-BIC as

$$M_N \ddot{y} + K_N y = 0. \tag{24}$$

We then determine the inherent properties of MDOF-BICs by setting the determinant of $K_N - M_N \omega^2$ to zero. We find that only the star model and fully connected model have inherent properties similar to the TDOF-BIC. They have two unequal natural frequencies and damping ratios, and their modal shapes have the same form.

The proof process is as follows. First, only for the success models, we have the values of q_{ij} and p_{ij} as

$$\begin{cases} q_{ij} = 1 & i,j = 1,\dots,N;\ i \neq j \\ p_i = p_j = p & i,j = 1,\dots,N. \end{cases}$$

Then the determinant of $K_N - M_N \omega^2$ as

$$\begin{vmatrix} k_m & k_3 & & k_3 \\ k_3 & k_m & & k_3 \\ & & \ddots & \\ k_3 & k_3 & & k_m \end{vmatrix} = \begin{vmatrix} k_n + Nk_3 & (N-1)k_3 & & k_3 \\ 0 & k_n & & 0 \\ & & \ddots & \\ 0 & 0 & & k_n \end{vmatrix} \tag{25}$$

where

- $k_m = k + pk_3 - m\omega^2$
- $k_n = k + (p-1)k_3 - m\omega^2$
- $p = 1$ for the star model and $p = N - 1$ for the fully connected model.

So we get the natural frequencies, damping ratios and modal shapes of the success models as

$$\omega_{1,2,\dots,N-1}^2 = \frac{k + (p-1)k_3}{m}, \ \omega_N^2 = \frac{k + (N+p-1)k_3}{m} \tag{26}$$

$$\zeta_{1,2,\dots,N-1}^2 = \frac{c + (p-1)c_3}{2\omega_1 m}, \ \zeta_N^2 = \frac{c + (N+p-1)c_3}{2\omega_N m} \tag{27}$$

$$\Phi = \frac{1}{\sqrt{2m}}$$

$$\times \begin{bmatrix} 1 & \frac{1}{\sqrt{3}} & \frac{1}{\sqrt{6}} & \cdots & \frac{1}{\sqrt{(N-1)N/2}} & \frac{1}{\sqrt{N/2}} \\ -1 & \frac{1}{\sqrt{3}} & \frac{1}{\sqrt{6}} & \cdots & \frac{1}{\sqrt{(N-1)N/2}} & \frac{1}{\sqrt{N/2}} \\ 0 & \frac{-2}{\sqrt{3}} & \frac{1}{\sqrt{6}} & \cdots & \frac{1}{\sqrt{(N-1)N/2}} & \frac{1}{\sqrt{N/2}} \\ 0 & 0 & \frac{-3}{\sqrt{6}} & \ddots & \vdots & \vdots \\ \vdots & \vdots & \vdots & \vdots & \frac{1}{\sqrt{(N-1)N/2}} & \frac{1}{\sqrt{N/2}} \\ 0 & 0 & 0 & \cdots & \frac{-(N-1)}{\sqrt{(N-1)N/2}} & \frac{1}{\sqrt{N/2}} \end{bmatrix}_{N \times N}. \tag{28}$$

The success models of MDOF-BIC degenerate into TDOF-BIC if n equals 2. This also proves that the star model and the fully connected model are the correct expansion methods. Meanwhile, the other failure models (chain, ring and combined model) prove that the effect of the model is non-ideal when the number of the unequal natural frequencies is unequal to 2. In summary, we conclude the criterion for multidimensional expansion is that the system has only two unequal natural frequencies.

4.3. System block diagram and simulation system of the MDOF-BIC

To construct the simulation system of the success MDOF-BIC systems, we need to first export its system block diagram. Similar to the method used to obtain the block diagram of the TDOF-BIC in section 2.2, we perform the Fourier transform of formula (23) and use the modal decomposition method in the frequency domain

$$Y_1(\omega) = \sum_{i=1}^{N} \Phi_{1i} \frac{\sum_{j=1}^{N} \Phi_{ji} X_j(\omega)}{\omega_i^2 - \omega^2 + 2i\omega_i \zeta_i \omega}$$

$$Y_2(\omega) = \sum_{i=1}^{N} \Phi_{2i} \frac{\sum_{j=1}^{N} \Phi_{ji} X_j(\omega)}{\omega_i^2 - \omega^2 + 2i\omega_i \zeta_i \omega}$$

$$\vdots$$

$$Y_N(\omega) = \sum_{i=1}^{N} \Phi_{Ni} \frac{\sum_{j=1}^{N} \Phi_{ji} X_j(\omega)}{\omega_i^2 - \omega^2 + 2i\omega_i \zeta_i \omega} \tag{29}$$

where Φ_{ji} is the element in jth row and ith column of the matrix Φ. Further, we summarize the matrix form of (29) as

$$\boldsymbol{Y}(\omega) = \boldsymbol{\Phi}\boldsymbol{H}(\omega) \odot \boldsymbol{\Phi}^\mathrm{T} \boldsymbol{X}(\omega) \tag{30}$$

where

- $\boldsymbol{H}(\omega) = [H_1(\omega) \ H_2(\omega) \ \cdots \ H_N(\omega)]^\mathrm{T}$
- $H_i(\omega) = (\omega_i^2 - \omega^2 + 2i\omega_i \zeta_i \omega)^{-1}$
- $\odot$ represents the Hadamard product.

Based on (30), we plot the block diagram of the MDOF-BIC in figure 13(take $N = 4$ as an example). Then, we use Simulink to model and simulate this block diagram and show them in figures 14(model) and 15 (result). We take the fully connected model as an example, and the simulation results are basically the same as figure 10(b), which verifies the correctness of the system block diagram.

4.4. Optimization of the success models

We now optimize the two success models. The star model has a poor magnification effect on the first and last spacing intervals. We achieve the optimization of it by extrapolating the input signals. For an arbitrary time t, we regard the N inputs as the N-point sampling in space

$$x_n(t) = x_t(n) = \exp\left[-i\left(\omega t + \varphi_1 - (n-1)\Delta\tau\right)\right] + e(t) \tag{31}$$

where φ_1 represents the phase of the first antenna, n represents the spatial sampling serial number.
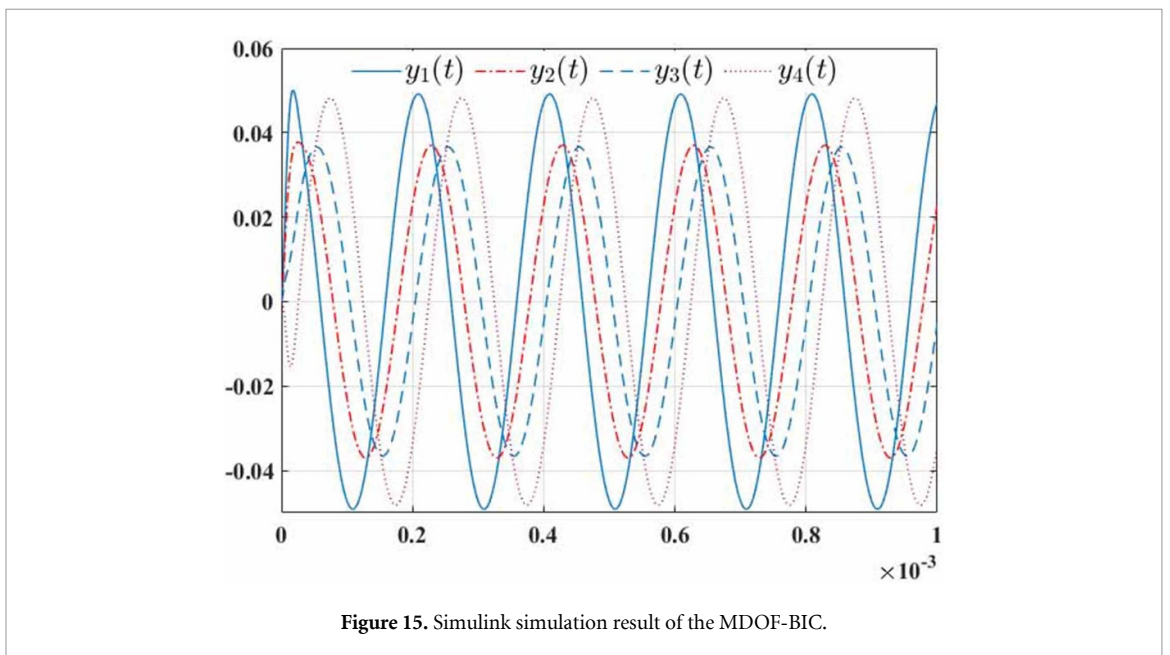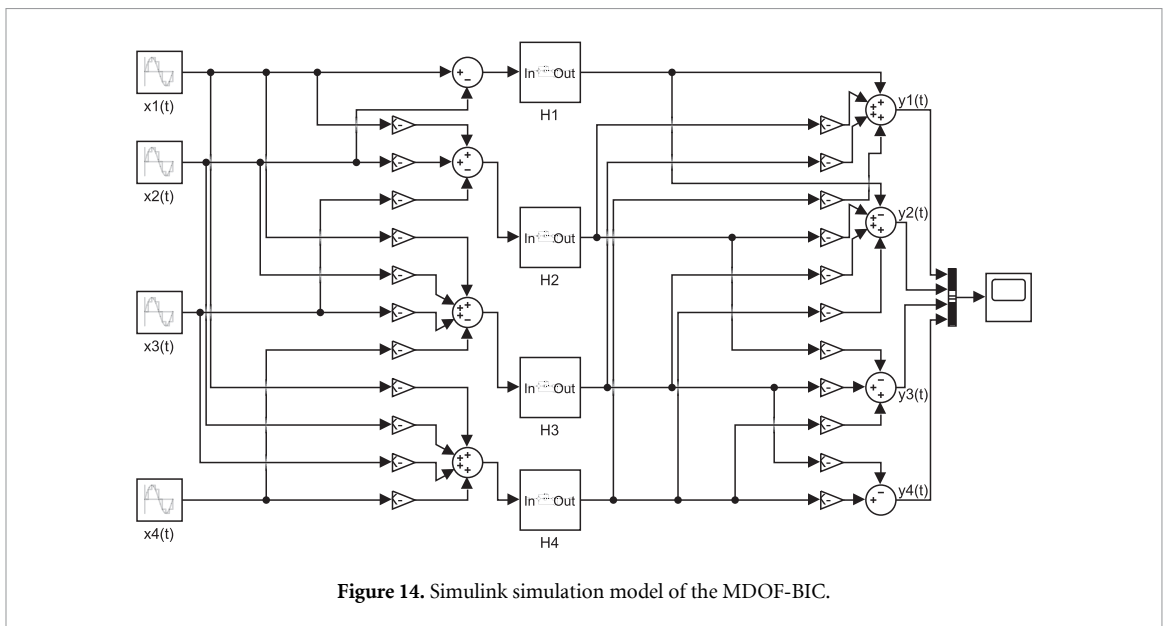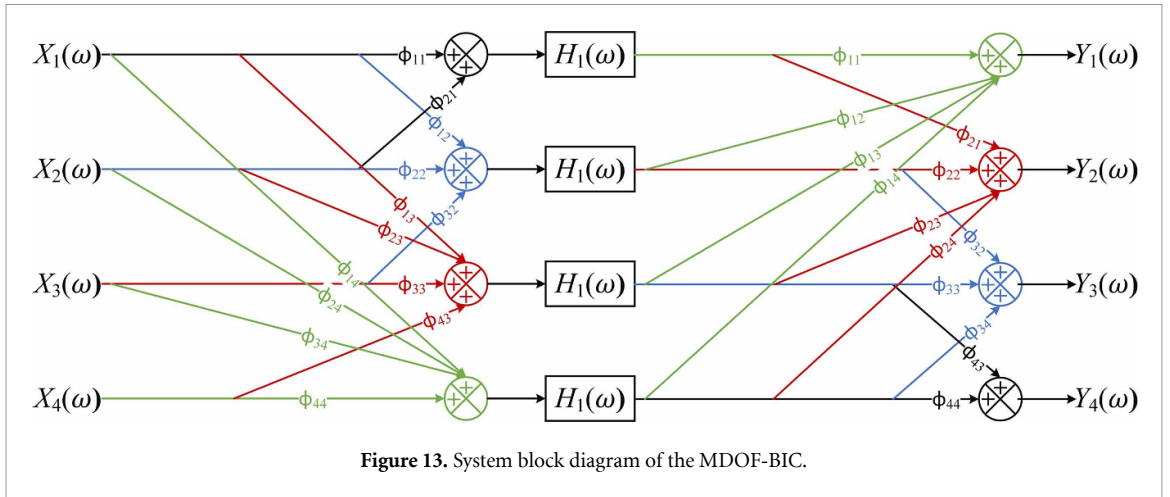
There is a clear exponential relationship between the inputs and the spatial sampling serial number, so we choose the exponential curve method as the extrapolation model.

$$x_t(n) = x_0 e^{Kn} \tag{32}$$

where the coefficients x_0 and K are obtained from the known data.

For an N-dimensional MDOF-BIC, we use forward and backward predictions to extrapolate one data point to each end. Then we have $N+2$ inputs, and the original first and last spacing interval becomes the second and penultimate intervals. By processing through an $N+2$-dimensional MDOF-BIC, we obtain $N+2$ responses. Select the middle N responses as the final result, then we overcome the shortcomings of the star model.

The deficiency of the fully connected model is the low response amplitudes. Inspired by (22), we find that MDOF-BIC still has the property: the amplitudes of the responses are unaffected by the change of the mass term, but immensely affected by the change of the stiffness term. We adjust the response amplitude to the required level by using the same scaling constant to change the system parameters. Note that this method does not affect the inherent properties of the system.

Figure 13. System block diagram of the MDOF-BIC.

Figure 14. Simulink simulation model of the MDOF-BIC.

Figure 15. Simulink simulation result of the MDOF-BIC.

Table 1. Values of the system parameters.

	Standard value	Initial value	Optimal value
m/kg	2.88×10^{-10}	2.88×10^{-16}	1.54×10^{-16}
c/Ns·m^{-1}	1.15×10^{-5}	1.30×10^{-8}	1.41×10^{-8}
c_3/Ns·m^{-1}	2.88×10^{-5}	2.88×10^{-8}	3.09×10^{-8}
k/N·m^{-1}	0.576	0.576	0.799
k_3/N·m^{-1}	5.18	5.18	5.84
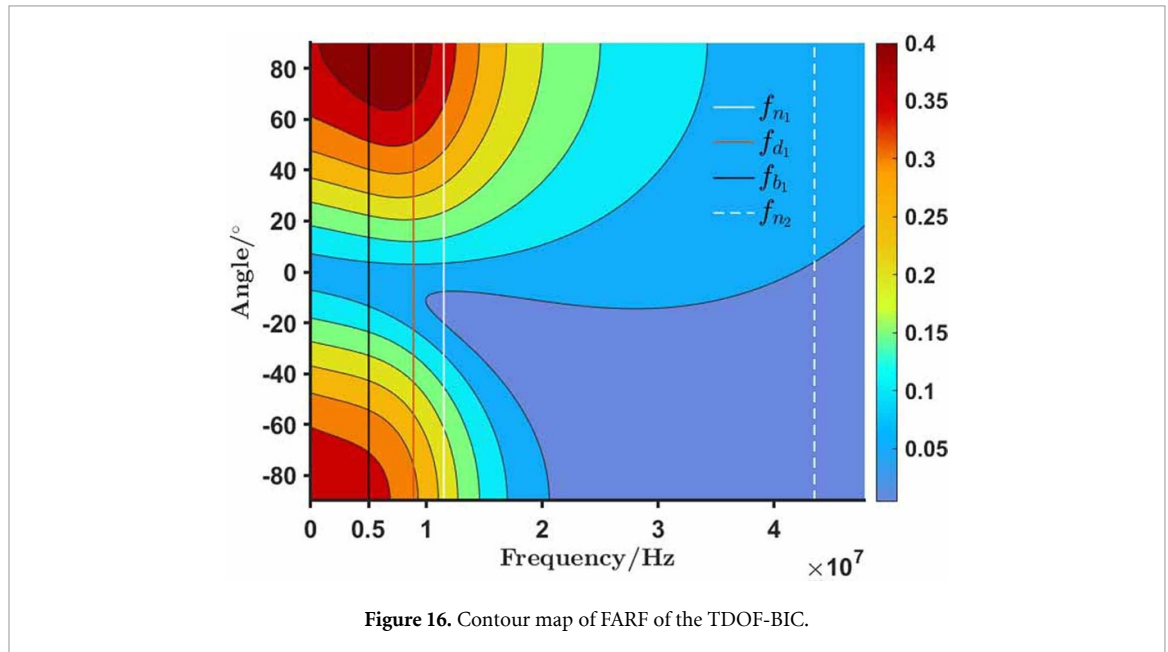
Figure 16. Contour map of FARF of the TDOF-BIC.

5. Numerical and experimental results

5.1. Numerical results

By the numerical simulation, we verify the frequency conversion algorithm and compare the aperture of the inspired arrays and ordinary array. By the inspired arrays we refer to arrays with MDOF-BIC systems. We also demonstrate the optimization of the two success models. The simulation is conducted under a common HFSWR scenario with the following parameters

- Frequency of operation, $f = 5$ MHz.
- Uniform linear array with 4 dipole antenna.
- Antenna spacing, $d = 0.1\lambda$.

We first adjust the system parameters to meet the desired frequency following the algorithm proposed in (21) and give the results in table 1. Use the optimal parameters, figures 16 and 17 depict the contour map of FARF and slice map of PDF, respectively. We observe that the available band has been converted from kHz to MHz band, and the first maximum response frequency f_{b_1} aligns with our desired frequency (see figure 16). In figure 17, we observe that the phase difference at f_{b_1} is steeper and f_{b_1} is farther away from f_j (compared with figure 8(b)).

Figure 18 compares the radiation patterns of the inspired arrays and ordinary array to clarify the illustrate the virtual aperture extension ability of the MDOF-BIC. It is evident that the inspired arrays outperform the ordinary array regarding the side-lobe suppression and main lobe width. This improvement in the radiation performance confirms that the MDOF-BIC has amplified the phase differences (time differences) between the received signals of the antennas, thereby achieving the virtual aperture extension of the array. Note that the inspired array with the star model exhibits better performance than the inspired array with the fully connected model. We can determine the model depend on the actual scenario.

Figure 19 presents the radiation pattern of the inspired arrays with the star model and optimized star model. We observe that the array with the optimized star model has a narrower main lobe width, validating the effectiveness of our optimization scheme.

To enhance the response amplitude of the fully connected model, we reduce the optimal system parameters by a factor of 10. Figure 20 illustrates the time-domain response of the fully connected model MDOF-BIC. The signal is incident from $30°$. We demonstrate the successful optimization of the fully connected model, as the response amplitude has increased tenfold.
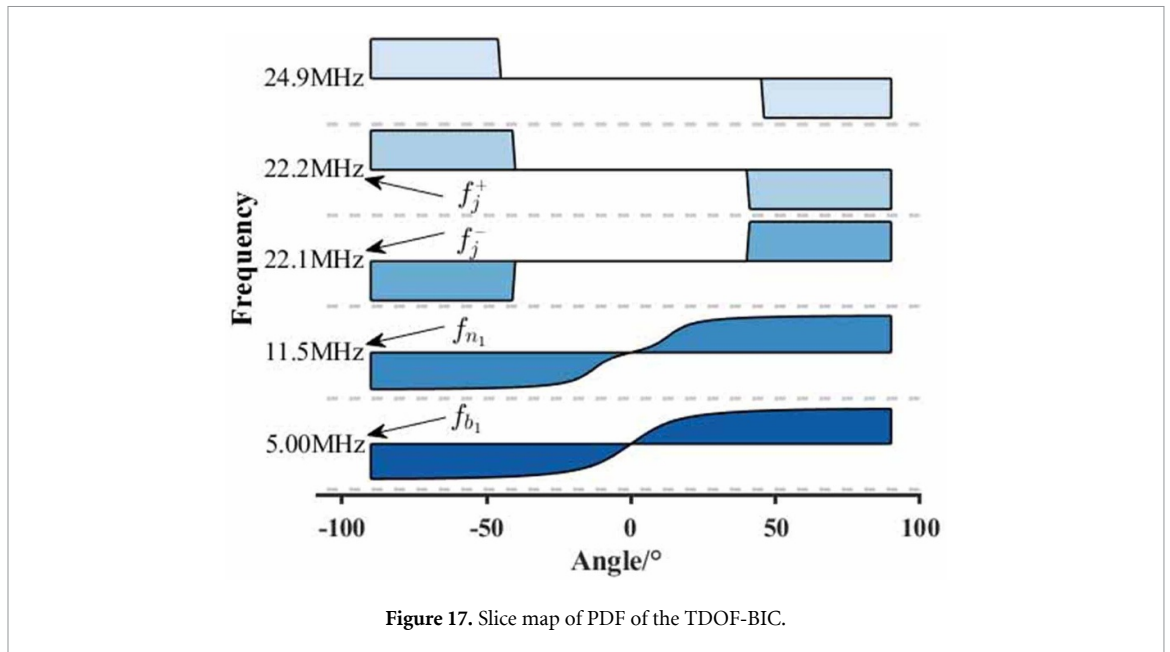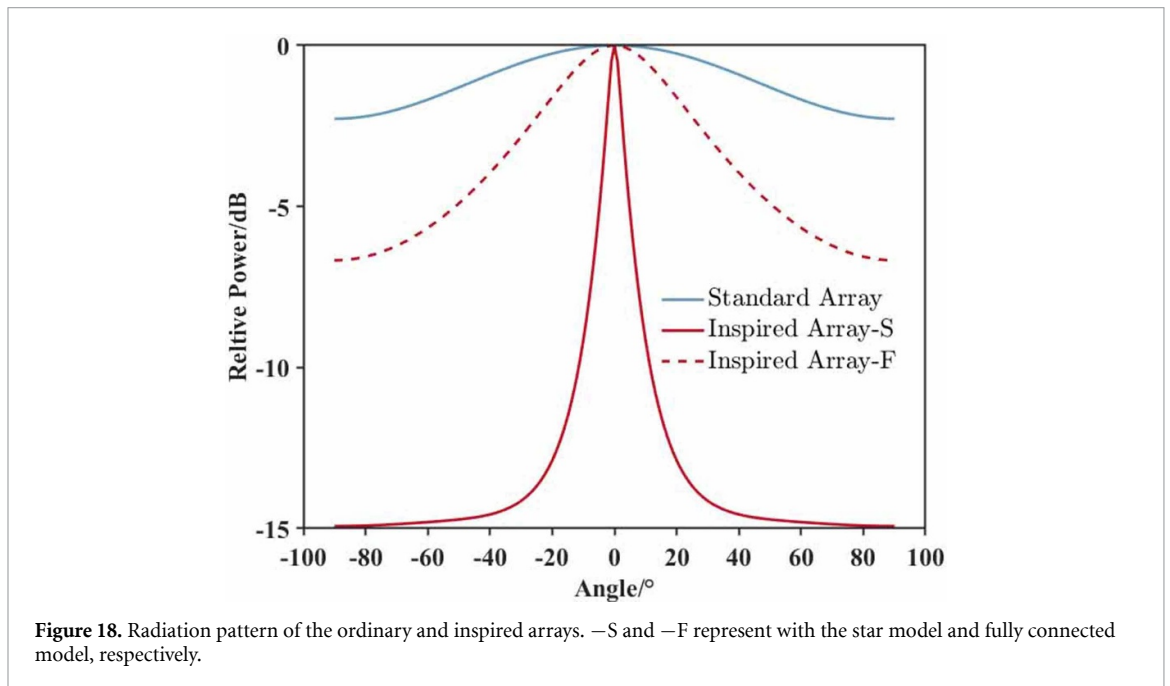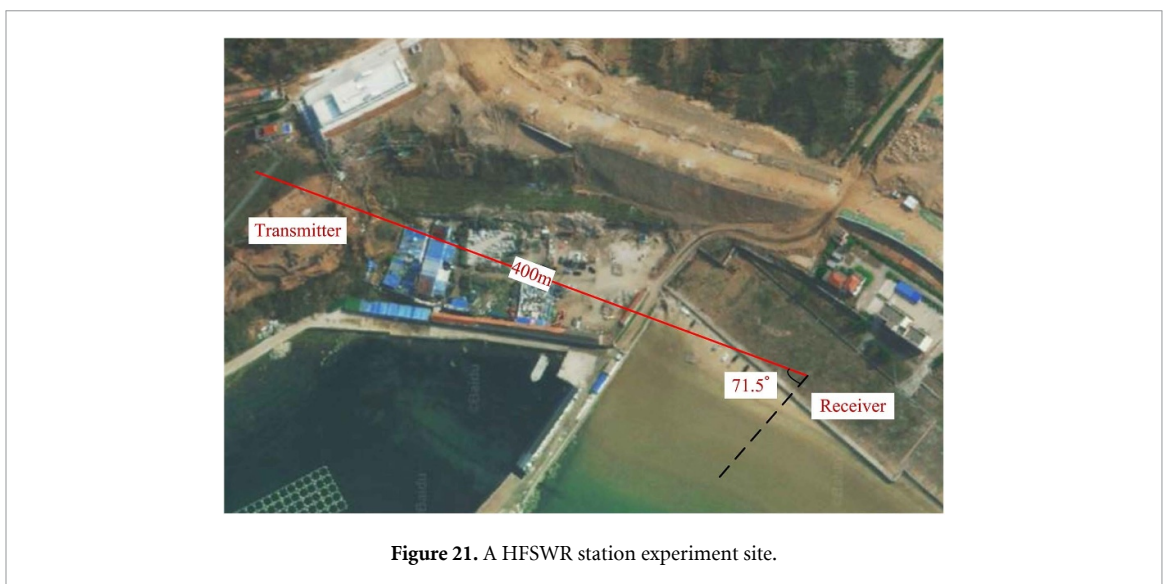
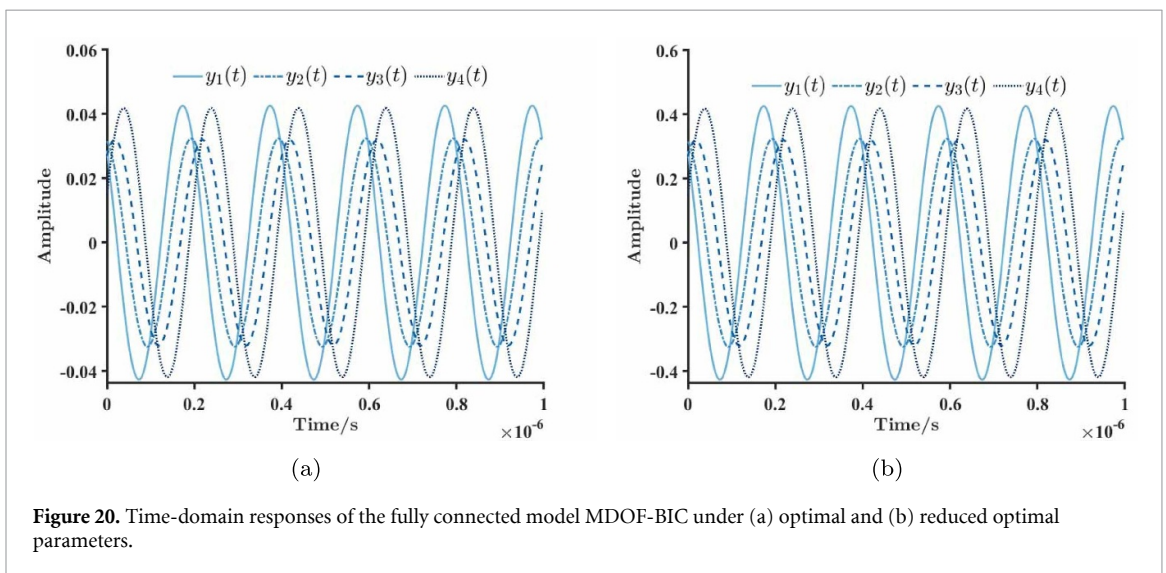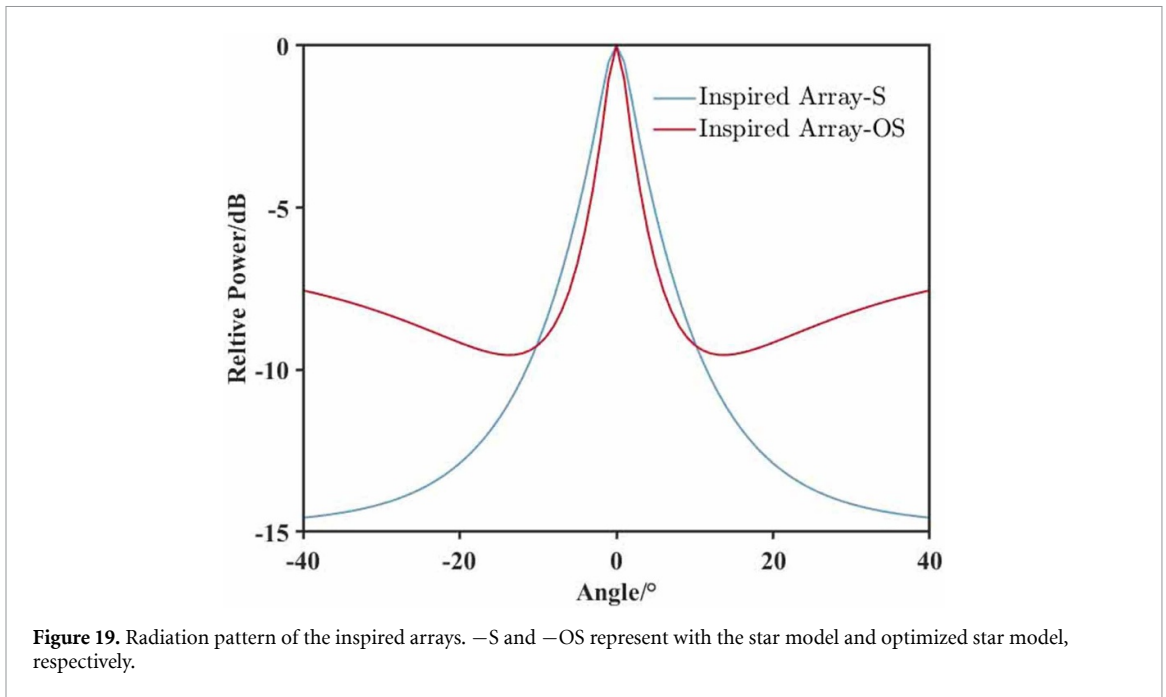**Figure 17.** Slice map of PDF of the TDOF-BIC.

Figure 18. Radiation pattern of the ordinary and inspired arrays. −S and −F represent with the star model and fully connected model, respectively.
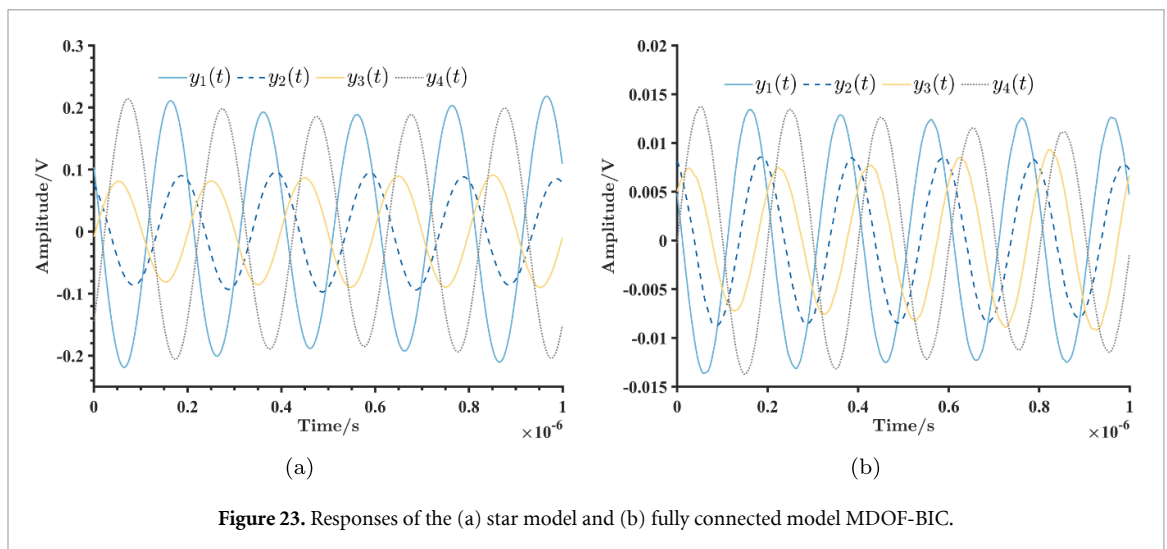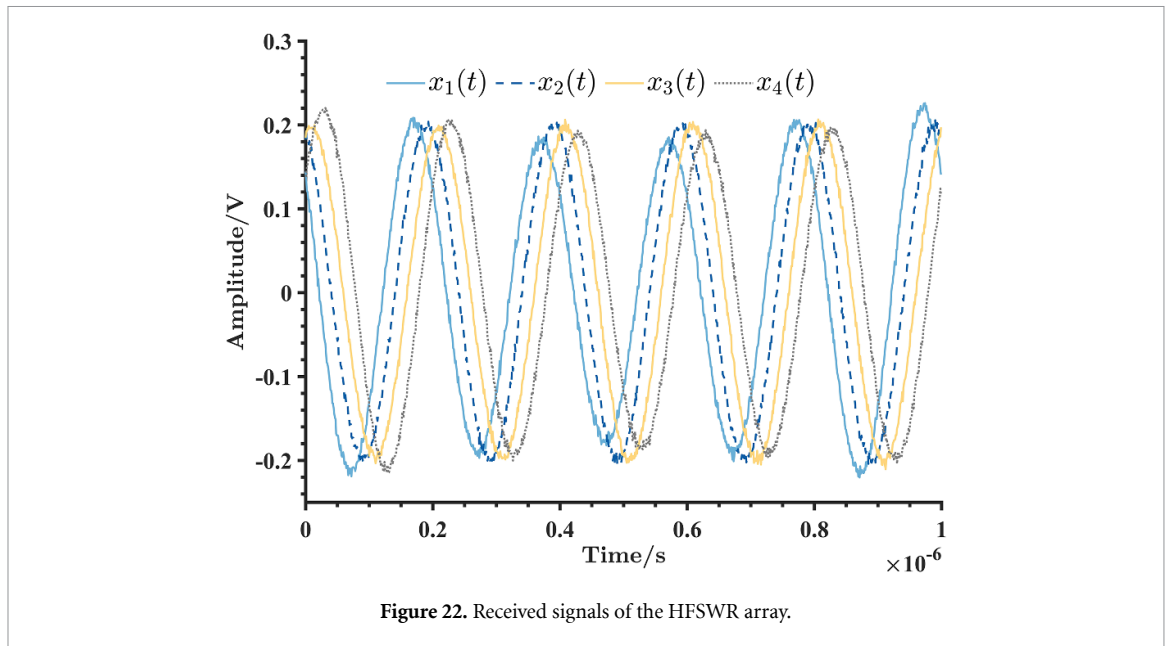
5.2. Experimental results

To demonstrate the practicability of the MDOF-BICs, we use them to process the actual signals received by the HFSWR array. The experimental site is a HFSWR station shown in figure 21. We utilize a log-period antenna to transmit a single frequency signal of 5MHz and four magnetic antennas with antenna spacing $d = 0.1\lambda$ to receive the signal. The distance between the transmitting station and the receiving station is about 400 meters (about 6.7λ), which satisfies the far field radiation condition. The signal is emitted from 71.5° relative to the normal of the array plane.

The transmitted power of the signal is 500 W, and the received signal of the array is shown in figure 22. Due to the influence of the noise and external signals, the received signal has some amplitude jitter and burr. Figure 23 shows the responses of the star and the fully connected model MDOF-BIC. It can be seen from the results that the two successful models also have good performance under the actual application. Both of them can realize the amplification of the phase difference, or say the virtual expansion of the aperture. In addition, the responses in figure 23 have no amplitude burr, which means that the BIC processing has improved the signal-to-noise ratios of the signals.

Figure 19. Radiation pattern of the inspired arrays. −S and −OS represent with the star model and optimized star model, respectively.

Figure 20. Time-domain responses of the fully connected model MDOF-BIC under (a) optimal and (b) reduced optimal parameters.

Figure 21. A HFSWR station experiment site.

Figure 22. Received signals of the HFSWR array.

(a)

(b)

Figure 23. Responses of the (a) star model and (b) fully connected model MDOF-BIC.

This additional advantage of the MDOF-BIC system comes from the filtering effect of the system.

6. Conclusion

We designed a virtual aperture extension method for the small aperture HFSWR multielement array inspired by the coupled auditory system of *Ormia Ochracea*. First, by mimicking the *Ormia*'s ears, we implemented a TDOF-BIC system and analyzed its extension ability to the array aperture. We regarded this aperture expansion as the generation of a virtual array and established the received signal model of the virtual array. Then, we analyzed the frequency response characteristics and determined the available frequency band of the TDOF-BIC. Based on this analysis, we proposed a frequency conversion algorithm to convert the available frequency band to the desired frequencies. To suit the multielement array, we extended TDOF to MDOF and proposed several models

of the MDOF-BIC. By solving their responses and natural properties, we finally determined two successful models and summarized the criteria for the successful extension. We also optimized the two successful models to address their respective shortcomings. We demonstrated the proposed frequency conversion algorithm and provided the optimal parameters for 5 MHz HFSWR. Through comparing the radiation patterns between the inspired arrays and the ordinary array, we verified that the MDOF-BIC can extend the virtual aperture of the array. The processing of the actual received signal of the array also demonstrated the validity of our proposed method.

Data availability statement

All data that support the findings of this study are included within the article (and any supplementary files).

Acknowledgments

ORCID iD

Hongbo Li ⓘ https://orcid.org/0000-0003-2427-7736

References

[1] Zheng J, Yang T, Liu H, Su T and Wan L 2020 *IEEE Trans. Ind. Inform.* **17** 5059–67
[2] Wan L, Liu K, Liang Y C and Zhu T 2021 *IEEE Trans. Wirel. Commun.* **20** 3152–67
[3] Shu T, He J and Dakulagi V 2021 *IEEE Trans. Aerosp. Electron. Syst.* **58** 180–8
[4] Krim H and Viberg M 1996 *IEEE Signal Process. Mag.* **13** 67–94
[5] Schmidt R 1986 *IEEE Trans. Antennas Propag.* **34** 276–80
[6] Robert D, Amoroso J and Hoy R R 1992 *Science* **258** 1135–7
[7] Miles R, Robert D and Hoy R 1995 *J. Acoust. Soc. Am.* **98** 3059–70
[8] Behdad N, Al-Joumayly M A and Li M 2011 *IEEE Antennas Wirel. Propag. Lett.* **10** 361–4
[9] Elfrgani A M and Rojas R G 2016 *IEEE Trans. Antennas Propag.* **64** 4297–305
[10] Grüner P, Chaloun T and Waldschmidt C 2018 *IEEE Trans. Antennas Propag.* **67** 1630–9
[11] Grüner P, Dorsch I and Waldschmidt C 2020 *IEEE Trans. Antennas Propag.* **69** 3899–912
[12] Jelodar A, Soleimani M and Sedighy S H 2020 *Iran. J. Electr. Electron. Eng.* **16** 130–6
[13] Dorsch I, Grüner P, Klose M, Schmucker D and Waldschmidt C 2021 *IEEE Trans. Microw. Theory Tech.* **69** 5173–84
[14] Akcakaya M and Nehorai A 2010 *Bioinspir. Biomim.* **5** 046003
[15] Akcakaya M, Muravchik C H and Nehorai A 2010 *2010 Conf. Record of the 44th Asilomar Conf. on Signals, Systems and Computers* pp 1961–5
[16] Akcakaya M, Muravchik C H and Nehorai A 2011 *IEEE Trans. Signal Process.* **59** 4795–808
[17] Akcakaya M, Muravchik C H and Nehorai A 2011 *2011 IEEE Int. Symp. on Antennas and Propagation (APSURSI)* pp 1530–3
[18] Singiresu S R *et al* 2016 *Mechanical Vibrations (5th Edition)* (Tsinghua University Press)